minerals

MDPI

Article

Region Expansion of a Hyperspectral-Based Mineral Map Using Random Forest Classification with Multispectral Data

Hideki Tsubomatsu and Hideyuki Tonooka *

Graduate School of Science and Engineering, Ibaraki University, Hitachi 3168511, Japan
* Correspondence: hideyuki.tonooka.dr@vc.ibaraki.ac.jp

Abstract: Observation images from hyperspectral (HS) sensors on satellites and aircraft can be used to map minerals in greater detail than those from multispectral (MS) sensors. However, the coverage of HS images is much less than that of MS images, so there are often cases where MS images cover the entire area of interest while HS images cover only a part of it. In this study, we propose a new method to more reasonably expand the mineral map of an HS image with an MS image in such cases. The method uses various mineral indices from the MS image and MS sensor's band values as the input and HS image-based mineral classes as the output. Random forest (RF) two-class classification is then applied iteratively to determine the distribution of each mineral in turn, starting with the minerals that are most consistent with the HS image-based mineral map. The method also involves the correction of misalignment between HS and MS images and the selection of input variables by RF multiclass classification. The method was evaluated in comparison with other methods in the Cuprite area, Nevada, using the Airborne Visible/Infrared Imaging Spectrometer (AVIRIS) and Hyperspectral Imager Suite (HISUI) as HS sensors and the Advanced Spaceborne Thermal Emission and Reflection Radiometer (ASTER) as MS sensors. As a result, all of the evaluated region-expansion methods with an HS–MS image pair, including the proposed method, showed better performance than the method using only an MS image. The proposed method had the highest performance, and the inter-mineral averages of the F1-scores for the overlap and non-overlap areas were 85.98% and 46.46% for the AVIRIS–ASTER image pair and 82.78% and 42.60% for the HISUI–ASTER image pair, respectively. Although the performance in the non-overlap region was lower than in the overlap region, the method showed high precision and high accuracy for almost all minerals, including minerals with only a few pixels. Misalignment between the HS–MS images is a factor that degrades accuracy and requires precise alignment, but the misalignment correction in the proposed method could suppress the effect of misalignment. Validation studies using different regions and different sensors will be carried out in the future.

Keywords: remote sensing; hyperspectral image; multispectral image; mineral mapping; random forest; classifier; mineral index; AVIRIS; HISUI; ASTER

check for updates

Citation: Tsubomatsu, H.; Tonooka, H. Region Expansion of a Hyperspectral-Based Mineral Map Using Random Forest Classification with Multispectral Data. *Minerals* **2023**, *13*, 754. https://doi.org/10.3390/min13060754

Academic Editors: Behnam Sadeghi, François R. Doucet, Marc Constantin and Christophe Germay

Received: 17 March 2023
Revised: 20 May 2023
Accepted: 29 May 2023
Published: 31 May 2023

Copyright: © 2023 by the authors. Licensee MDPI, Basel, Switzerland. This article is an open access article distributed under the terms and conditions of the Creative Commons Attribution (CC BY) license (https://creativecommons.org/licenses/by/4.0/).

1. Introduction

Optical remote sensing is a valuable tool for efficiently determining the wide-area distribution of minerals. Multispectral (MS) sensors, which have multiple spectral bands in the visible to thermal infrared region, have been a widely used sensor type for mineral mapping [1,2], and typical examples include the Landsat sensors such as the Thematic Mapper (TM) and Operational Land Imager (OLI) [3,4] as well as the Advanced Spaceborne Thermal Emission and Reflection Radiometer (ASTER) [5] aboard the Terra satellite. In particular, many minerals are known to have specific absorption characteristics in the short-wavelength infrared (SWIR) range, and despite the relatively low spectral resolution of MS sensors, there have been numerous reports of effective mineral identification through analysis of SWIR images taken with these sensors. For example, Rowan et al. successfully mapped resource-useful minerals such as muscovite and dolomite in Mountain Pass,

California, USA, using band ratio analysis based on ASTER images [6]. Vural et al. also mapped minerals via principal component analysis based on Landsat-7 and -8 images using samples collected in northeastern Turkey [7]. Thus, MS sensors are widely used for mineral mapping, but it has also been reported that some minerals are difficult to identify due to limitations in the number of bands and wavelength resolution [8–10]. Mars et al. compared ASTER image spectra from two alteration areas (e.g., Cuprite, Nevada, and Mountain Pass, California, USA) with a spectral library and, based on the results of spectral matching, identified some mineral groups, including argillic minerals (kaolinite, alunite, and dickite), phyllic alteration minerals (sericite), propylitic minerals (calcite, epidote, and chlorite), and other advanced mineral groups, that could be separated [11]. However, the study also concluded that detailed mapping of kaolinite and alunite was impossible due to the similarity of the minerals and the limited number of bands in the multispectral sensor.

On the other hand, hyperspectral (HS) sensors, which have significantly more bands than MS sensors, as they typically range from fifty to several hundred spectral bands, enable the detailed mapping of minerals. Typical HS sensors include the Airborne Visible/Infrared Imaging Spectrometer (AVIRIS) [12], Environmental Monitoring and Analysis Program (EnMap) [13], PRecursore IperSpettrale della Missione Applicativa (PRISMA) [14], and Hyperspectral Imager Suite (HISUI) [15]. In addition, the development of NASA's Surface Biology and Geology (SBG) [16], ESA's Copernicus Hyperspectral Imaging Mission for the Environment (CHIME) [17], and other similar initiatives with planned launches in the late 2020s is indicative of the global attention directed towards advancing HS sensor technology. However, fewer HS sensors have been operated than MS sensors, and they generally have narrower swath widths, resulting in fewer available data archives and more unobserved areas. For example, the HISUI, which was installed on the International Space Station (ISS) in 2019, has a constrained orbit and does not have pointing capability; thus, it is assumed that many unobserved areas will remain after the mission is over [15].

To address this problem, attempts have been made to expand the mineral mapping area of the limited HS images by using MS images covering a wider ground surface area. For example, Kruse and Perry [18] performed minimum noise factor (MNF) transformations [19] and pixel purity index (PPI) analysis [20] for atmospherically corrected HS images, then extracted the endmember spectra necessary for identifying each mineral based on n-dimensional scatter plots [20] and obtained endmember spectra from MS images by multiplying the extracted spectra with the spectral response functions of the MS sensor's bands. These endmember spectra were applied to the atmospherically corrected MS image, and then the spectral angle mapper (SAM) method [21] was applied to generate a mineral map in the missing region of the HS image (hereinafter referred to as the KP method). However, since the KP method is subject to mineral classification errors when there are spectral inconsistencies between HS and MS images due to radiometric calibration errors or atmospheric correction errors, Hirai and Tonooka [22,23] proposed a modified method that is robust to these effects (hereinafter referred to as the "HT method"). The HT method extracts endmember pixels of each mineral from the HS image in the overlap region between the HS and MS images, using the same methods [18–20] as the KP method. Then, MS-based endmember spectra are extracted from the pixels in the MS image at the exact locations of the HS-based endmember pixels. This method cannot be affected by spectral inconsistencies between HS and MS images. However, it also causes errors in mineral identification if there is a misalignment between HS and MS images [22]. Therefore, Nakayama and Tonooka [24] proposed an improved HT method that determines MS-based endmember pixels from the neighborhood of the endmember pixels on the HS image and also optimizes the mineral selection by the SAM method. The features of this improved HT method are that it is robust to misalignment between HS and MS images and can automatically set threshold values for each mineral.

These region expansion methods for HS-based mineral maps are intended to produce a seamless mineral map of the entire region of interest more accurately than processing MS images alone by utilizing information from partially available HS images when MS

images cover the entire region of interest but HS images are partially missing. These methods extract the endmember pixels of each mineral from the HS image obtained in a portion of the region of interest, but the difference is that the KP method calculates the MS-based endmember spectrum from the HS-based endmember spectrum, while the HT and improved HT methods use the HS-based endmember location information. Based on this background, the present study proposes a new method with the same objective but a different approach from these region expansion methods. The proposed method builds a machine learning model to obtain the best-fit mineral identification results from MS images for those from HS images in the overlap region and applies it to the entire region of interest. The method was validated at Cuprite, Nevada, USA, using AVIRIS and HISUI images as HS images and ASTER images as MS images, and its effectiveness was demonstrated.

2. Materials and Methods

2.1. Proposed Method

The proposed method performs mineral identification by iteratively applying a random forest (RF) two-class classification (that is, a two-class classification of the target mineral or not) to the MS image to maximize the consistency between the mineral map of the HS image and that of the MS image in the overlap region. The variables to be input into the RF two-class classification were selected from the band values of the MS sensor, and the major mineral indices were based on the band calculations through iterative multiclass classification by RF. RF was chosen as the machine learning method in this study because it has demonstrated superior performance compared to other classification methods in multiclass classification tasks using remote sensing data [25].

The details of this method are described below, and the flow is shown in Figure 1.

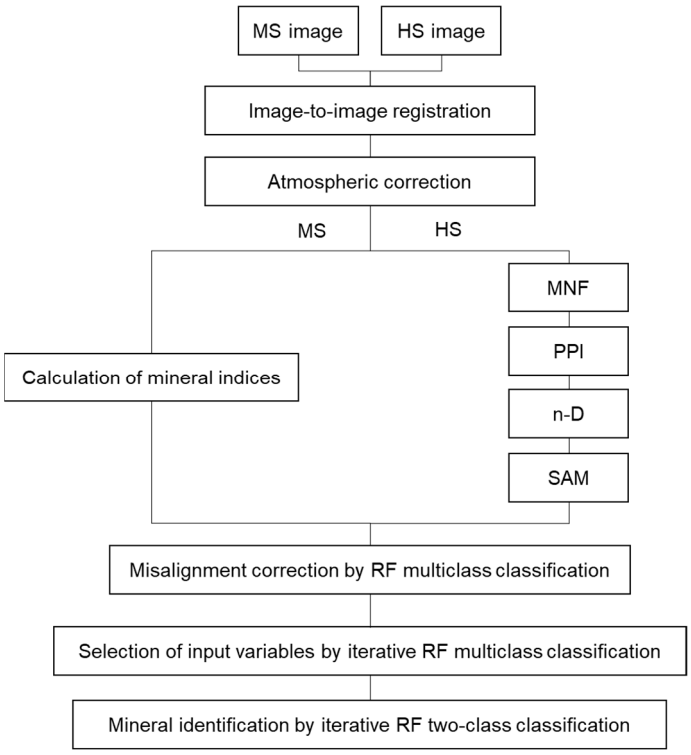


Figure 1. Processing flow of the proposed method.

2.1.1. Step 1: Preprocessing

As a preprocessing step, HS and MS images of the target area were prepared and aligned. In addition, to improve the performance of mineral identification, the HS and MS images used were atmospherically corrected.

2.1.2. Step 2: Mineral Mapping from HS Images

Mineral classification maps were generated from HS images by the following general procedures: (1) data compression of HS images by MNF transformation [19], (2) extraction of pure pixels by PPI analysis of MNF-transformed images [20], (3) extraction of endmember pixels using a multidimensional correlation diagram [20], (4) determination of each endmember spectrum and corresponding mineral by comparison with a spectral library [20], and (5) mineral identification of each pixel by the spectral angle mapper (SAM) method [18,26]. Although the accuracy of the mineral map produced by this method depends on the quality of the satellite imagery and the type of minerals present, some have achieved 90% or better discrimination accuracy for certain minerals when using ground-validated reference data [27]. In general, it can be expected that HS mineral maps, while not necessarily true, are more reliable than MS mineral maps produced using the same method.

2.1.3. Step 3: Misalignment Correction by RF Multiclass Classification

The proposed method assumes that there is no misalignment between HS and MS images, and if this is not satisfied, the accuracy of mineral classification may be significantly reduced. Therefore, the following process was used to correct misalignment between HS and MS images.

First, based on the MS sensor used, some candidate mineral indices based on band calculations were prepared. Then, in the HS–MS overlap region, an RF multiclass classifier was trained with these mineral indices and the band values as input variables and the mineral classes obtained in Step 2 as output variables, and the overall accuracy was calculated. Then, the position of the HS image relative to the MS image was shifted within the range where the amount of pixel shift in parallel is assumed (e.g., eight neighborhoods), and the overall accuracy of the RF multiclass classifier was calculated for each shift value. The shift value that shows the highest overall accuracy was then adopted, and the position of the HS image was corrected.

Since the above misalignment correction is a method of shifting the entire image in parallel based on the assumption that the amount of misalignment is uniform across the entire image, the accuracy may be locally degraded if this assumption is not met.

2.1.4. Step 4: Selection of Input Variables by Iterative RF Multiclass Classification

In the RF multiclass classification of Step 3, all the prepared mineral indices and band values were used. However, the ideal state of RF is one in which the correlation of groups of decision trees is low among each other, and the presence of highly correlated decision trees may reduce generalizability due to overfitting. Therefore, the following process was performed in the overlapping regions to select the mineral indices and band values to be used as input variables. First, the overall accuracy based on the shift value adopted in Step 3 was used as the criterion. Then, one of the input variables was selected, and the RF multiclass classifier was trained by removing that variable to calculate the overall accuracy. If its value was higher than the criterion, the variable was removed. This process was performed for all variables in turn. In this way, the final remaining variables were used as the input variables to be given to the following RF two-class classifier.

2.1.5. Step 5: Mineral Identification by Iterative RF Two-Class Classification

In the overlap region, with the mineral indices and band values from Step 4 as input variables and the mineral classes from Step 2 as output variables, the RF two-class classifier was trained for each of the N target minerals, and its accuracy (F1-score) was calculated. Then, the mineral with the highest accuracy (designated as Mineral 1) was selected, and the model learned for that mineral was applied to the entire MS image, including the non-overlapping area, to determine the Mineral 1 pixel. Next, for all remaining pixels (unidentified pixels) in the overlap region, except for the pixels determined to be Mineral 1, the same two-class classification prediction process was performed for each target

mineral except for Mineral 1, and the mineral with the highest accuracy (designated as Mineral 2) was determined. The classifier was then applied to the unidentified pixels in the MS image to determine the pixels belonging to Mineral 2, completing the identification of Mineral 2. After that, the same process was applied iteratively to complete the identification of all target minerals sequentially. In this case, the number of learning RF runs in Step 5 was N times for N target minerals, the number of predictions in the overlap region was N(N + 1)/2 times, and the number of predictions in the region, including the MS extension region, was N times.

2.2. Study Area and Data Used

2.2.1. Study Area

In this research, the study area was the Cuprite area in Nevada, USA, which is often used for empirical studies in geological remote sensing [28,29]. The location of this area is shown in Figure 2. It is known that minerals with characteristic absorption properties in the SWIR region are well exposed in this area [30]. In addition, a surface reflectance reference map of the hills known as the Cuprite hills and example spectra obtained from them were reported in [31].

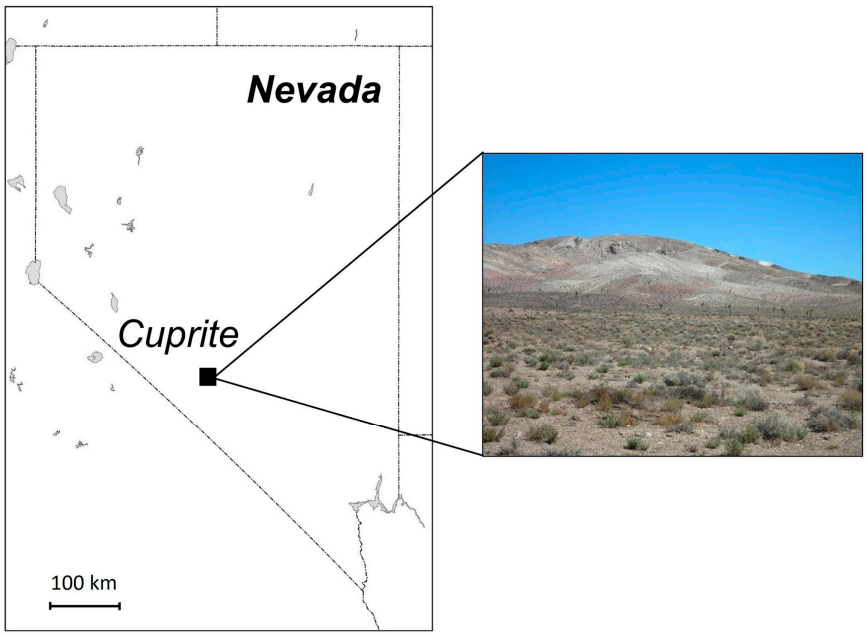


Figure 2. Cuprite area, Nevada, USA, used as the study area.

2.2.2. HS and MS Images Used

In this study, AVIRIS and HISUI images were used as HS images, and ASTER images were used as MS images. Table 1 lists the images used.

Table 1. List of remote sensing images used.

Type	Sensor	Date and Time (UTC)	Spatial Resolution (m)	Product ID
HS sensor	AVIRIS HISUI	20 September 2006 19:21 5 April 2021 20:02	15.7 20	f060920t01p00r05 HSHL1G_N376W1172_20210405200234_20221208052533
MS sensor	ASTER	15 August 2006 18:38	VNIR: 15 SWIR: 30 TIR: 90	AST_07XT_00308152006183834_20230424001733_7858 AST_L1T_00308152006183834_201 50515181406_80216

AVIRIS is an airborne HS sensor developed by the NASA Jet Propulsion Laboratory (JPL) and has been in operation since 1986 [5,32]. It has 224 spectral bands in the visible and near-infrared (VNIR) and SWIR spectral regions (0.360–2.510 µm). The basic specifications of AVIRIS are given in Table 2. The AVIRIS data used in this study include an image taken on 20 September 2006 in the Cuprite area at a ground resolution of 15.7 m that was obtained from the NASA AVIRIS Data Portal [33]. SWIR bands from 175 to 224 (wavelength range: 2.020–2.510 µm) were used for this analysis.

Table 2. Basic specifications of AVIRIS [32].

Subsystem	Band	Spectral Range (µm)	Spatial Resolution (m)	Signal Quantization Levels (bits)
VNIR	1–96	0.360–1.259	4–20	12
SWIR	97–224	1.260–2.510		

HISUI is a Japanese HS sensor launched on 5 December 2019 that is attached to the Japanese Experiment Module (JEM) of the ISS, with 185 bands in the VNIR and SWIR spectral regions (0.405–2.475 µm) [34]. Table 3 shows the basic specifications of HISUI. The HISUI data used in this study include an image taken in the Cuprite area on 5 April 2021, and the ground resolution of the product is 20 m. SWIR bands from 147 to 185 (wavelength range: 2.000–2.475 µm) were used for this analysis. Note that this HISUI image contains a few clouds and their shadows. These contaminated areas were masked based on their peculiar spectral characteristics and excluded from the validation.

Table 3. Basic specifications of HISUI [34].

Subsystem	Band	Spectral Range (µm)	Spatial Resolution (m)	Signal Quantization Levels (bits)
VNIR	1–57	0.405–0.965	20–31	12
SWIR	58–185	0.970–2.475		

ASTER is an MS sensor developed by the Japanese Ministry of Economy, Trade, and Industry (METI) onboard NASA's Terra satellite, which was launched in December 1999 and is still in operation as of March 2023. It has VNIR, SWIR, and thermal infrared (TIR) subsystems, with three bands for VNIR, six for SWIR, and five for TIR, and it has a ground resolution of 15 m for VNIR, 30 m for SWIR, and 90 m for TIR. Table 4 shows the basic specifications of ASTER. For the AVIRIS and HISUI images, only the SWIR bands were used, but for ASTER images, all VNIR, SWIR, and TIR bands were used for this analysis. In this study, two kinds of ASTER products, which were acquired on August 15 2006 over the Cuprite area, were used: the ASTER/07XT Surface Reflectance VNIR and Crosstalk-Corrected SWIR (AST_07XT) product [35] for VNIR and SWIR, and the ASTER/Level 1T (L1T) ortho-rectified at-sensor radiance product for TIR. The ASTER/07XT is a product that has been atmospherically corrected and converted to surface reflectance, where the SWIR images in the product have been corrected for inter-band crosstalk that affects spectral analysis [36]. For TIR, the ASTER L1T TIR images were first recalibrated [37] and then corrected atmospherically by the water vapor scaling (WVS) method [38]. The surface temperature and five-band surface emissivity images were acquired by the ASTER temperature and emissivity separation (TES) algorithm [39] and used for analysis.

Table 4. Basic specifications of ASTER [39].

Subsystem	Band	Spectral Range (μm)	Spatial Resolution (m)	Signal Quantization Levels (bits)
VNIR	1	0.520–0.600	15	8
	2	0.630–0.690		
	3N/3B	0.760–0.860		
SWIR	4	1.600–1.700	30	
	5	2.145–2.185		
	6	2.185–2.225		
	7	2.235–2.285		
	8	2.295–2.365		
	9	2.360–2.430		
TIR	10	8.125–8.475	90	12
	11	8.475–8.825		
	12	8.925–9.275		
	13	10.25–10.95		
	14	10.95–11.65		

2.3. Validation Method

2.3.1. Methods to Be Compared

In this study, the proposed method was validated by comparing two alternative methods with some modifications of the proposed method, the improved HT method, and an MS-based method without any HS images.

The first alternative method is to omit Section 2.1.5 and identify minerals with a multiclass RF classifier using the input variables selected in Step 4. This method is more straightforward than the proposed method and has the advantage of a shorter processing time. Herein, this method will be referred to as method A.

The second alternative method is a method that performs multiclass classification by RF instead of two-class classification by RF in Section 2.1.5. The input variables in the RF classifier in Step 5 were the same as in the proposed method, but the output values were all mineral classes obtained in Step 2. Then, only the mineral with the highest prediction F1-score (which is designated as Mineral 1) in the overlap region was considered to have completed identification. Then, using only the unidentified pixels in the MS image, the RF multiclass classifier for minerals other than Mineral 1 was trained again to determine the mineral with the highest prediction F1-score (Mineral 2); the identification of Mineral 2 was completed based on this. In the same manner, after that, all minerals were identified sequentially. In this case, the number of training and predicting RF runs in Step 5 is N times for N minerals. Herein, this method will be referred to as method B.

The improved HT method selects the best MS-based endmember pixel from around the MS pixel at the exact location as the HS-based endmember pixel in the overlap region between the HS and MS images to obtain the MS endmember spectrum [24]. Then, the mineral of each pixel is identified by the SAM method given the obtained MS endmember spectra.

The MS-based method does not use HS images but applies the procedure of Section 2.1.2 to the ASTER band images (surface reflectance for VNIR and SWIR and surface emissivity for TIR) to create mineral maps. This method was compared to evaluate the effectiveness of the region expansion of the HS-based mineral map, which is the objective of the other methods.

2.3.2. Application of the Methods

In Section 2.1.1, initial geocoding of the AVIRIS, HISUI, and ASTER images was performed based on the location information attached to each product. For the AVIRIS and HISUI images, observed radiance values were atmospherically corrected by the atmospheric correction module FLAASH [39–42] of the ENVI 5.6 software and converted to surface reflectance, where the atmospheric model was US Standard, the aerosol model was Rural,

and the date and time data and geometric conditions were given based on the attribute information of each image.

Step 2 was processed by the ENVI 5.6 software, and the threshold of the SAM method was set to the default value (=0.1).

In Step 3, considering that the sensor used in this study was ASTER, the 32 mineral (or mineral class) indices for ASTER [5,6,43–52] shown in Table 5, 14 band values (9 surface reflectance values for VNIR and SWIR and 5 surface emissivity values for TIR), and 1 surface temperature value were used as input variables. In Step 4, these 47 input variables (32 mineral indices + 14 band values + 1 temperature value) were used as candidates, and the mineral numbers on the HS-based mineral map were used as output variables to remove unnecessary variables.

Table 5. ASTER-based mineral indices were prepared as input variables for Step 3 and input variable candidates for Step 4. This table was created by merging Tables 2 and 3 from Gozzard (2006) [45] and partially appending information from Table 2 from Rajendran et al. (2019) [46]. Table courtesy of Geological Survey and Resource Strategy Division, Department of Mines, Industry Regulation and Safety. © State of Western Australia 2023.

No.	ASTER Band Math	Features	Comments	Reference
1	2/1	Ferric iron, Fe^{3+} discrimination (blue)	—	Rowan et al., 2003 [6] Hewson et al., 2001 [48] Abrams et al., 1995 [5]
2	(5/3) + (1/2)	Ferric iron, Fe^{2+}	—	Rowan et al., 2003 [6]
3	4/5	Laterite alteration	—	Bierwith, 2002 [43] Volesky et al., 2003 [47]
4	4/2	Gossan	—	Volesky et al., 2003 [47]
5	5/4	Ferrous silicates (biotite, chlorite, amphibole)	Fe oxide Cu–Au alteration	Hewson et al., 2001 [48]
6	4/3	Ferric oxide discrimination (green)	Can be ambiguous	Hewson et al., 2001 [48] Abrams et al., 1995 [5]
7	(7 + 9)/8	Carbonate–chlorite–epidote	—	Rowan et al., 2003 [6]
8	(6 + 9)/(7 + 8)	Epidote–chlorite–amphibole	Endoskarn	Hewson et al., 2001 [48]
9	(6 + 9)/8	Amphibole–MgOH	Can be either MgOH or carbonate	Hewson et al., 2001 [48]
10	6/8	Amphibole	—	Bierwith, 2002 [43]
11	(6 + 8)/7	Dolomite	—	Rowan et al., 2003 [6]
12	13/14	Carbonate	Exoskarn (calcite–dolomite)	Bierwith, 2002 [43] Ninomiya, 2002 [49] Hewson et al., 2001 [48]
13	(5 + 7)/6	Sericite–muscovite–illite–smectite	Phyllic alteration	Rowan et al., 2003 [6] Hewson et al., 2001 [48]
14	(4 + 6)/5	Alunite–kaolinite–pyrophyllite	—	Rowan et al., 2003 [6]
15	5/6	Phengite host rock	—	Hewson et al., 2001 [48] Volesky et al., 2003 [47]
16	7/6	Muscovite	—	Hewson et al., 2001 [48]
17	7/5	Kaolinite	Approximate only	Hewson et al., 2001 [48]
18	(5 × 7)/(6 × 6)	Clay	—	Bierwith, 2002 [43]
19	14/12	Quartz-rich rocks	—	Rowan et al., 2003 [6]
20	(11 × 11)/(10 × 12)	Silica siliceous rocks	—	Bierwith, 2002 [43] Ninomiya, 2002 [49]

Table 5. *Cont.*

No.	ASTER Band Math	Features	Comments	Reference
21	12/13	Mafic minerals SIO_2	Inversely correlated with SiO_2 content in silicate rocks	Bierwith, 2002 [43] Ninomiya, 2002 [49] Hewson et al., 2001 [48]
22	$(12 \times 12 \times 14)/(13 \times 13 \times 13)$	Mafic minerals (improved)	Inversely correlated with SiO_2 content in silicate rocks	Ninomiya, 2002 [49]
23	13/12	SIO_2	Same as 14/12	—
24	11/10	Silica	—	Hewson et al., 2001 [48]
25	11/12	Silica	—	Hewson et al., 2001 [48]
26	13/10	Silica	—	Hewson et al., 2001 [48]
27	3/2	Vegetation	—	—
28	$(3 - 2)/(3 + 2)$	NDVI	Normalized difference vegetation index	—
29	4/1	Discrimination for mapping (red)	—	—
30	3/1	Discrimination for mapping (green)	—	—
31	12/14	Discrimination for mapping (blue)	—	—
32	4/7	Discrimination (red)	—	Abrams et al., 1995 [5]

3. Results

3.1. Validation Results Using AVIRIS and ASTER Images

The HS-based mineral map obtained via Section 2.1.2 using AVIRIS images is shown in Figure 3a. A total of nine minerals were identified by this process, including alunite and muscovite. The white dotted box in the image's southern half was defined as the overlap area between the HS and MS images. The northern half of the image was assumed to be a non-overlap area. Although this region was actually covered by the AVIRIS image, we did not use it; rather, we identified minerals by each method using the ASTER image.

Table 6 shows the overall accuracy when the position of the AVIRIS image is shifted by ± 1 pixel in the x- and y-directions with respect to the ASTER image, according to Section 2.1.3. Since the highest overall accuracy was obtained for the center position ($\Delta x = \Delta y = 0$), no position correction was performed between the AVIRIS and ASTER images. As a result, the geocoding of Step 1 was adopted as is.

In Section 2.1.4, 8 of the 47 input values, including the 1, 2, and 10–14 band values, and the mineral index No. 24 in Table 5 were excluded, leaving 39 variables to be selected. In the proposed method and the alternative methods, these were used as input variables for the RF classification in Step 5. The same validation was also performed in the expanded region to show accuracy.

Figure 3b–f shows the mineral maps obtained by the proposed method, the two alternative methods, the improved HT method, and the MS-based method. The non-overlap area in the north was extended using the MS image in the overlap area in the south. Table 7 also shows the accuracy of each mineral obtained by each method, with precision, recall, and F1-score as evaluation measures, for each of the overlap and non-overlap regions. The bottom row shows the average values of precision and recall and the F1-score calculated from them for the nine identified minerals. Bold numbers in each measure indicate the highest number among the methods.

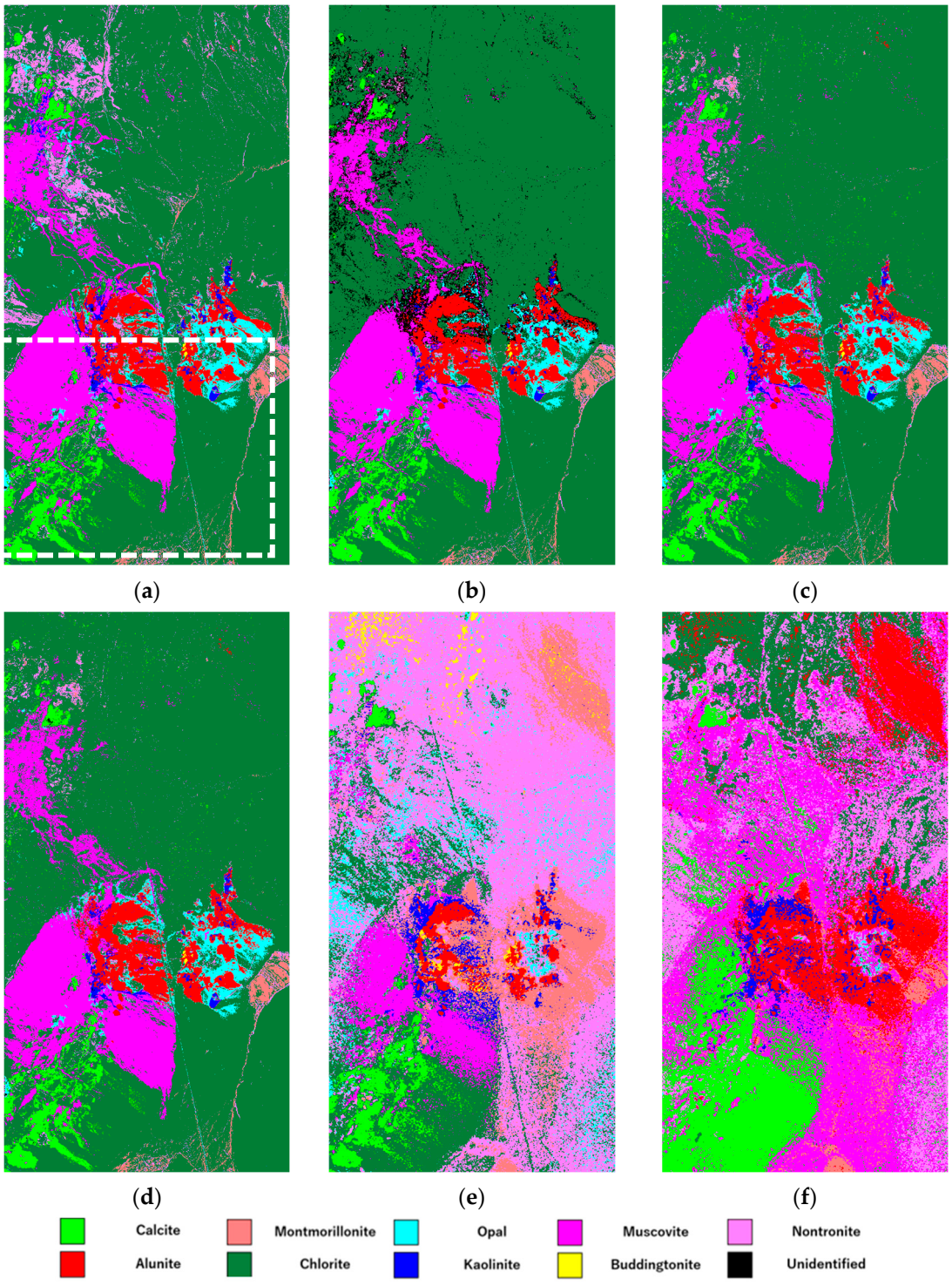


Figure 3. Comparison of mineral maps obtained from a single AVIRIS image and mineral maps from each of the extension methods using ASTER images: (**a**) AVIRIS-based map and the extended maps by (**b**) proposed method, (**c**) method A, (**d**) method B, (**e**) improved HT method, and (**f**) MS-based method. The white dotted box in (**a**) indicates the overlap region.

The proposed method has the highest precision for all minerals except alunite. The two alternative methods show similar results to each other. The improved HT method showed higher accuracy for alunite than the other methods, but the accuracy for some minerals was lower. In the non-overlap region, montmorillonite identification was low for all methods. The MS-based method had the lowest average F1-score of the methods.

Table 6. Overall accuracy when the position of the AVIRIS image was shifted by ±1 pixel in the *x*- and *y*-directions with respect to the ASTER image, according to Section 2.1.3. The bold number is the highest value.

	Δx = −1	**Δx = ±0**	**Δx = +1**
Δy = −1	81.93	83.21	81.77
Δy = ±0	83.20	**88.90**	83.29
Δy = +1	81.69	83.24	81.98

Table 7. Precision, recall, and F1-score for each mineral in the overlap and non-overlap regions for each method when the AVIRIS image was used as the HS image. The average values of precision and recall and the F1-score calculated from them are also shown in the bottom row. Bold numbers in each row indicate the highest number among the methods.

Mineral	**Measure**	**Proposed**		**Method A**		**Method B**		**Improved HT**		**MS-Based**	
		Overlap	**Non-Overlap**	**Overlap**	**Non-Overlap**	**Overlap**	**Non-Overlap**	**Overlap**	**Non-Overlap**	**Overlap**	**Non-Overlap**
Calcite	Precision	**99.28**	**79.01**	95.91	50.27	96.32	54.02	58.78	73.29	16.85	12.14
	Recall	**97.41**	42.97	97.35	49.84	97.29	47.56	71.46	50.63	93.34	**51.22**
	F1-score	**98.33**	55.67	96.62	50.05	96.80	50.58	64.51	**59.89**	28.55	19.63
Alunite	Precision	91.33	81.54	86.43	74.15	86.90	74.98	**91.64**	**91.75**	38.42	16.07
	Recall	81.86	65.21	**87.92**	**76.78**	87.49	75.98	41.77	35.08	72.05	67.39
	F1-score	86.34	72.47	87.17	75.44	**87.20**	**75.48**	57.38	50.75	50.11	25.95
Montmorillonite	Precision	**99.68**	**3.54**	97.47	2.25	97.67	2.47	5.28	0.60	13.66	2.51
	Recall	**84.76**	0.12	84.48	1.01	84.47	0.88	37.64	**10.11**	35.71	5.82
	F1-score	**91.62**	0.24	90.51	1.39	90.59	1.30	9.27	1.13	19.76	**3.51**
Chlorite	Precision	**96.14**	**87.63**	95.02	86.11	95.02	86.11	75.68	71.52	91.03	86.65
	Recall	94.78	92.21	**97.08**	**95.35**	**97.08**	**95.35**	29.77	8.27	4.01	24.66
	F1-score	95.45	89.86	**96.04**	**90.50**	**96.04**	**90.50**	42.73	14.82	7.68	38.40
Opal	Precision	**87.36**	**68.92**	75.92	53.54	75.62	53.19	8.22	5.76	43.85	27.44
	Recall	70.83	37.29	**77.27**	**48.13**	76.93	47.76	10.96	16.44	2.82	3.82
	F1-score	**78.23**	48.40	76.59	**50.69**	76.27	50.33	9.39	8.54	5.30	6.70
Kaolinite	Precision	**90.98**	**65.22**	78.37	48.50	79.84	50.27	20.84	25.14	20.33	23.16
	Recall	52.47	13.30	**57.17**	20.32	56.52	19.56	52.60	**42.75**	48.73	39.66
	F1-score	**66.56**	22.09	66.11	28.64	66.18	28.16	29.85	**31.66**	28.69	29.24
Muscovite	Precision	**94.24**	74.85	91.15	67.84	90.66	67.24	91.14	**86.73**	24.43	19.55
	Recall	93.38	63.47	94.06	68.37	**94.20**	**68.72**	56.41	26.74	50.28	66.75
	F1-score	**93.81**	**68.69**	92.58	68.10	92.40	67.97	69.69	40.88	32.88	30.24
Buddingtonite	Precision	**98.83**	**66.67**	87.44	26.47	92.97	35.00	5.37	0.24	0.00	0.00
	Recall	87.11	6.78	**89.69**	15.25	88.66	11.86	57.22	**33.90**	0.00	0.00
	F1-score	**92.60**	12.31	88.55	**19.35**	90.77	17.72	9.81	0.48	0.00	0.00
Nontronite	Precision	**99.74**	**64.90**	94.81	50.47	92.17	46.52	4.02	9.39	5.29	9.52
	Recall	42.44	1.80	41.67	6.67	41.35	7.26	**51.26**	**76.06**	28.71	30.34
	F1-score	**59.54**	3.50	57.89	11.78	57.09	12.56	7.46	**16.72**	8.94	14.49
All	Precision	**95.29**	**65.81**	89.17	51.07	89.69	52.20	40.11	40.49	28.21	21.89
	Recall	78.34	35.91	**80.74**	**42.41**	80.44	41.66	45.45	33.33	37.29	32.18
	F1-score	**85.98**	**46.46**	84.75	46.34	84.81	46.34	42.61	36.56	32.12	26.06

3.2. Validation Results Using HISUI and ASTER Images

The HS-based mineral map obtained via Section 2.1.2 using the HISUI image is shown in Figure 4a. The dummy region in the lower right is outside the observed area. A total of nine minerals were identified by this process, which is the same as the results obtained using the AVIRIS image. The white dotted box in the image's southern half was defined as the overlap area between the HS and MS image.

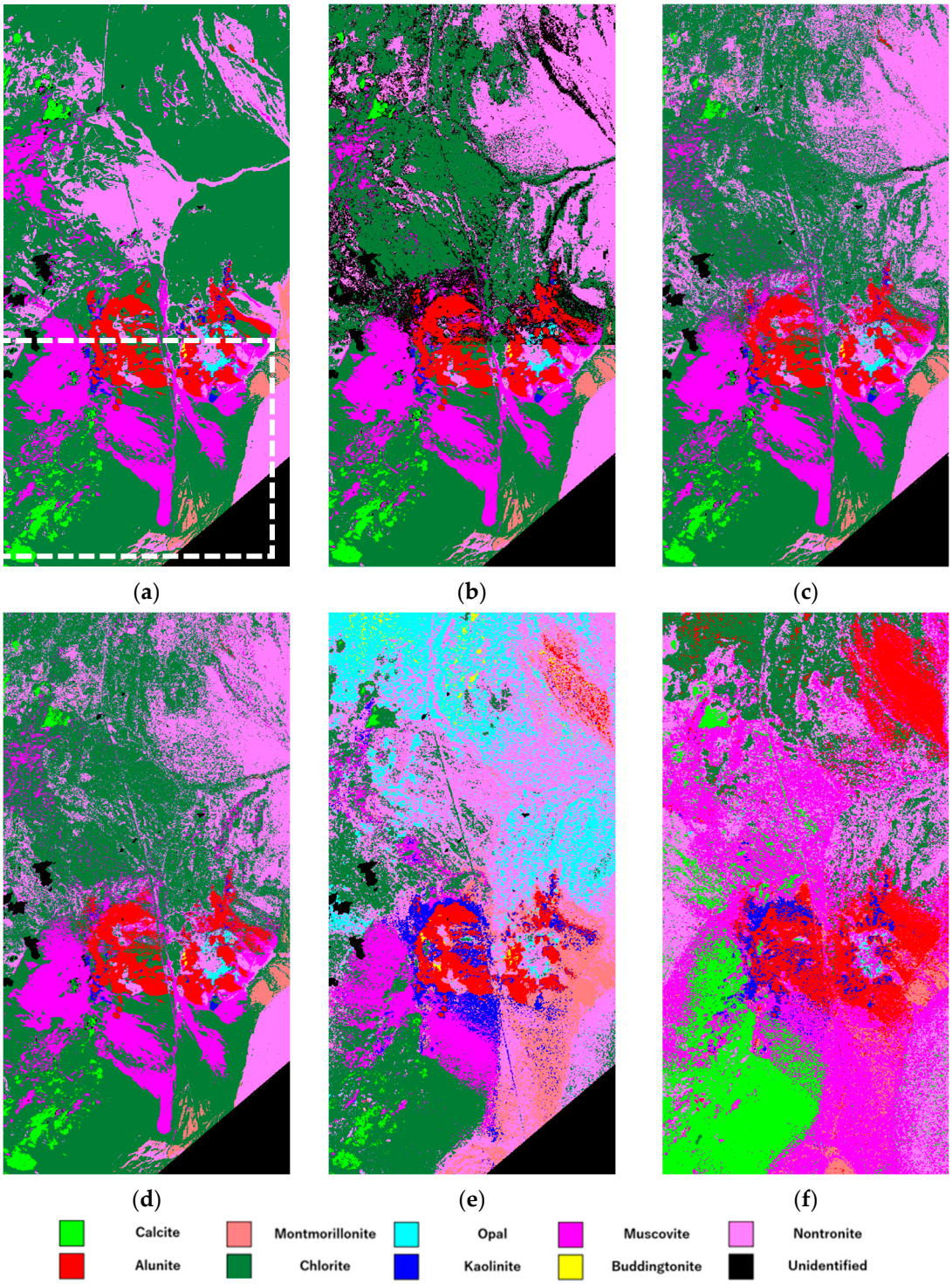


Figure 4. Comparison of mineral maps obtained from a single HISUI image and mineral maps from each of the extension methods using ASTER images: (**a**) HISUI-based map and the extended maps by (**b**) proposed method, (**c**) method A, (**d**) method B, (**e**) improved HT method, and (**f**) MS-based method. The white dotted box in (**a**) indicates the overlap region.

The overall accuracy when the position of the HISUI image was shifted ±1 pixel in the *x*- and *y*-directions with respect to the ASTER image in Section 2.1.3 is shown in Table 8. Since the highest overall accuracy was obtained at the center position ($\Delta x = \Delta y = 0$), no position correction was performed between the HISUI and ASTER images. Therefore, the geocoding of Step 1 was adopted as is.

Table 8. Overall accuracy when the position of the HISUI image was shifted by ±1 pixel in the *x*- and *y*-directions with respect to the ASTER image, according to Section 2.1.3. The bold number is the highest value.

	Δx = −1	**Δx = ±0**	**Δx = +1**
Δy = −1	62.41	64.47	62.44
Δy = ±0	63.79	**68.37**	62.96
Δy = +1	62.24	63.28	62.25

For Section 2.1.4, the 39 variables obtained from the analysis using the AVIRIS images discussed in Section 3.1 were used as input variables in the validation with the HISUI image as well. Figure 4b–f shows the mineral maps obtained by the five methods. Because the MS-based method does not depend on HS images, Figure 4f is the same as Figure 3f.

The validation results using the HISUI and ASTER combination are shown in Table 9. Precision is the highest for the proposed method for all minerals, and the two alternative methods show similar results to each other. The region of nontronite slightly above the center was not reproduced well by all methods, while the improved HT method showed better results for this mineral. The MS-based method had the lowest average F1-score of the methods.

Table 9. Precision, recall, and F1-score for each mineral in the overlap and non-overlap regions for each method when the HISUI image was used as the HS image. The average values of precision and recall and the F1-score calculated from them are also shown in the bottom row. Bold numbers in each row indicate the highest number among the methods.

Mineral	**Measure**	**Proposed**		**Method A**		**Method B**		**Improved HT**		**MS-Based**	
		Overlap	**Non-Overlap**	**Overlap**	**Non-Overlap**	**Overlap**	**Non-Overlap**	**Overlap**	**Non-Overlap**	**Overlap**	**Non-Overlap**
Calcite	Precision	**99.58**	**79.26**	96.90	56.90	96.90	50.51	73.77	79.14	7.57	9.18
	Recall	**98.50**	52.73	95.36	52.08	95.36	52.60	42.84	18.47	97.37	**66.66**
	F1-score	**99.03**	**63.33**	96.12	54.38	96.12	51.53	54.20	29.96	14.05	16.14
Alunite	Precision	**89.17**	**77.50**	83.14	66.76	83.33	67.45	83.60	63.57	35.40	14.03
	Recall	87.86	74.43	91.07	**78.71**	**91.22**	78.51	75.26	66.43	71.84	67.33
	F1-score	**88.51**	**75.93**	86.93	72.24	87.10	72.56	79.21	64.97	47.42	23.22
Montmorillonite	Precision	**98.50**	**39.65**	93.77	9.38	96.22	22.40	10.17	1.88	16.96	3.79
	Recall	**75.58**	7.80	73.83	12.14	73.43	13.86	54.23	**20.90**	35.77	10.96
	F1-score	**85.53**	13.04	82.61	10.59	83.29	**17.12**	17.12	3.45	23.01	5.63
Chlorite	Precision	**90.79**	67.65	87.00	67.03	86.46	66.33	76.18	60.29	87.94	**90.10**
	Recall	75.31	39.74	81.75	52.88	**82.30**	**52.98**	38.24	10.36	4.59	28.93
	F1-score	82.33	50.07	84.29	**59.12**	**84.33**	58.91	50.92	17.68	8.73	43.79
Opal	Precision	**79.15**	**46.39**	61.92	26.37	68.13	35.56	2.43	0.24	27.29	8.74
	Recall	77.29	43.57	**81.76**	**52.34**	77.76	47.31	31.72	37.27	18.71	20.33
	F1-score	**78.21**	**44.94**	70.47	35.07	72.62	40.60	4.51	0.48	22.20	12.23
Kaolinite	Precision	**86.63**	**36.34**	69.98	27.22	72.59	26.40	7.06	7.35	9.87	9.27
	Recall	53.26	8.89	56.57	18.53	55.60	14.89	**64.32**	**62.53**	50.49	47.11
	F1-score	**65.97**	14.29	62.56	**22.05**	62.97	19.04	12.73	13.15	16.51	15.49
Muscovite	Precision	**91.82**	54.06	83.30	33.59	83.32	30.88	70.94	**59.01**	20.02	12.99
	Recall	**87.71**	32.37	87.70	33.77	87.67	33.71	47.39	28.79	42.28	**57.65**
	F1-score	**89.72**	**40.49**	85.44	33.68	85.44	32.23	56.82	38.70	27.17	21.20
Buddingtonite	Precision	**97.83**	**40.00**	85.26	26.92	89.19	26.92	11.83	0.26	0.00	0.00
	Recall	**92.47**	15.38	91.10	53.85	90.41	53.85	61.64	**100.00**	0.00	0.00
	F1-score	**95.07**	22.22	88.08	**35.90**	89.80	**35.90**	19.85	0.52	0.00	0.00
Nontronite	Precision	**58.04**	19.34	54.25	23.52	54.73	22.67	31.84	**29.37**	21.37	19.43
	Recall	55.67	28.09	**60.31**	37.12	59.13	35.31	58.11	**57.68**	24.51	21.94
	F1-score	56.83	22.91	**57.12**	28.79	56.85	27.61	41.14	**38.92**	22.83	20.61
All	Precision	**87.95**	**51.13**	79.50	37.52	81.21	38.79	40.87	33.46	25.16	18.61
	Recall	78.18	33.67	**79.94**	43.49	79.21	42.56	52.64	**44.71**	38.40	35.66
	F1-score	**82.78**	**40.60**	79.72	40.29	80.20	40.59	46.01	38.27	30.40	24.46

3.3. Effect of Misalignment between AVIRIS and ASTER Images

Figure 5 shows the mineral map of each method when the AVIRIS and ASTER images were misaligned (two pixels to the bottom and one pixel to the right), and Table 10 shows the accuracy of each method. In the MS-based method, positional misalignment is irrelevant and is therefore not mentioned.

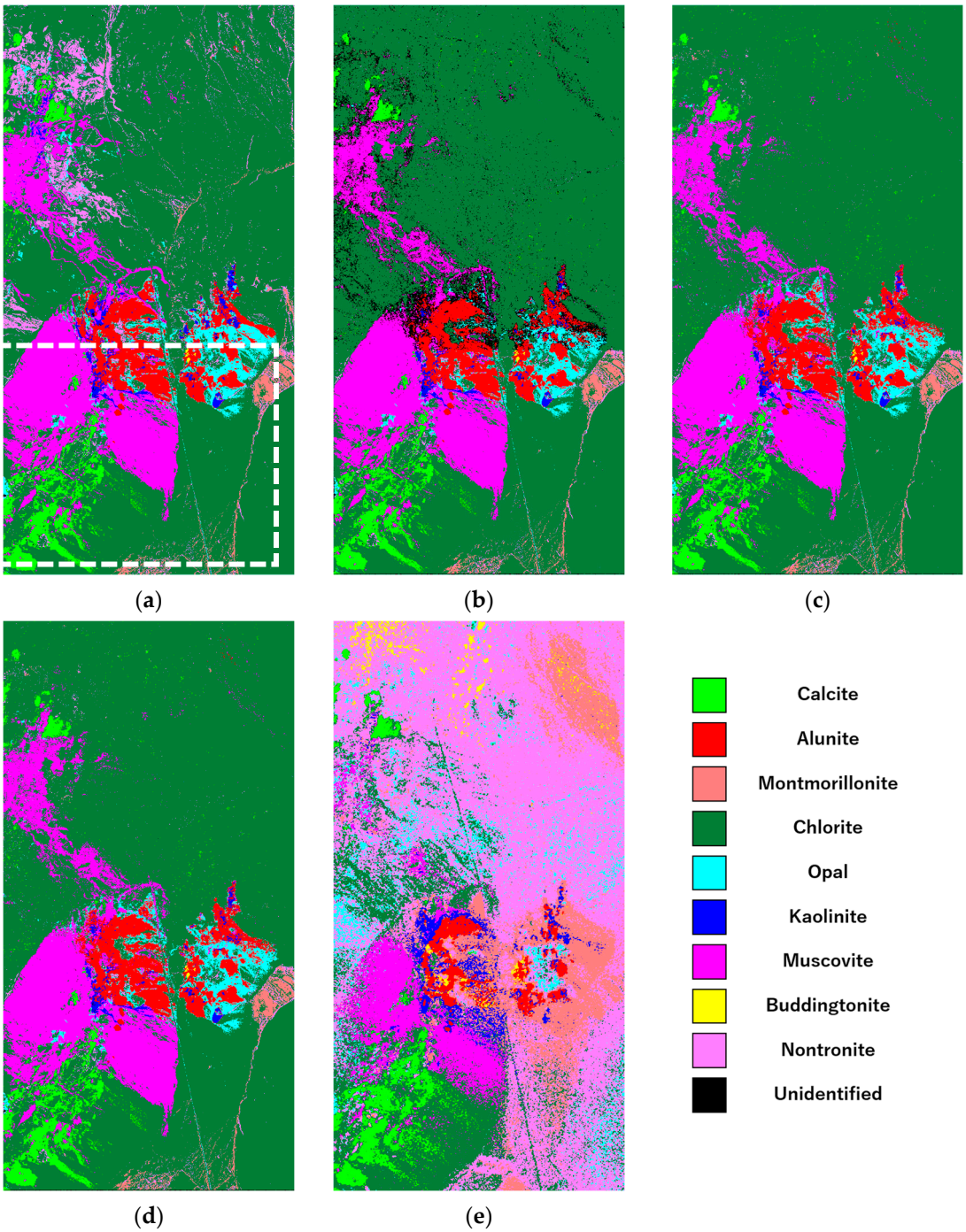


Figure 5. Mineral maps for the case of misalignment between AVIRIS and ASTER images: (**a**) AVIRIS-based map and the extended maps by (**b**) proposed method, (**c**) method A, (**d**) method B, and (**e**) improved HT method. The white dotted box in (**a**) indicates the overlap region.

Table 10. Precision, recall, and F1-score for each mineral in the overlap and non-overlap regions for each method for the case of misalignment between AVIRIS and ASTER images. The average values of precision and recall and the F1-score calculated from them are also shown in the bottom row. Bold numbers in each row indicate the highest number among the methods.

Mineral	Measure	Proposed		Method A		Method B		Improved HT	
		Overlap	Non-Overlap	Overlap	Non-Overlap	Overlap	Non-Overlap	Overlap	Non-Overlap
Calcite	Precision	**69.45**	61.83	68.11	52.03	68.23	53.41	58.78	**73.29**
	Recall	68.52	44.71	68.82	**51.78**	68.86	51.01	**71.46**	50.63
	F1-score	**68.98**	51.89	68.46	51.91	68.54	52.18	64.51	**59.89**
Alunite	Precision	82.34	79.15	77.82	71.55	78.29	72.35	**91.64**	**91.75**
	Recall	72.96	63.26	**80.69**	**77.90**	80.53	77.59	41.77	35.08
	F1-score	77.37	70.32	79.23	74.59	**79.39**	**74.88**	57.38	50.75
Montmorillonite	Precision	**52.38**	1.60	51.82	3.65	52.08	**3.95**	5.28	0.60
	Recall	44.73	0.09	**45.00**	0.64	45.07	0.46	37.64	**10.11**
	F1-score	48.25	0.17	48.17	1.09	**48.32**	0.82	9.27	**1.13**
Chlorite	Precision	**89.67**	**87.19**	88.72	85.62	88.72	85.62	75.68	71.52
	Recall	87.24	90.77	**90.60**	**95.69**	**90.60**	**95.69**	29.77	8.27
	F1-score	88.44	88.95	**89.65**	**90.38**	**89.65**	**90.38**	42.73	14.82
Opal	Precision	**64.91**	**68.30**	59.08	54.02	58.80	53.49	8.22	5.76
	Recall	47.70	30.28	55.53	42.62	**56.15**	**43.66**	10.96	16.44
	F1-score	54.99	41.96	57.25	47.64	**57.44**	**48.08**	9.39	8.54
Kaolinite	Precision	**57.35**	**63.55**	53.92	51.03	53.71	50.45	20.84	25.14
	Recall	30.85	10.23	35.73	16.76	35.87	16.93	**52.60**	**42.75**
	F1-score	40.12	17.62	42.98	25.23	**43.02**	25.36	29.85	**31.66**
Muscovite	Precision	84.35	71.33	82.00	66.18	82.10	66.41	**91.14**	**86.73**
	Recall	84.77	65.47	85.85	**70.90**	**85.86**	70.75	56.41	26.74
	F1-score	**84.56**	68.28	83.88	68.46	83.94	**68.51**	69.69	40.88
Buddingtonite	Precision	**54.43**	16.67	51.43	**25.00**	50.89	11.11	5.37	0.24
	Recall	44.33	1.69	46.39	10.17	44.33	3.39	**57.22**	**33.90**
	F1-score	**48.86**	3.08	48.78	**14.46**	47.38	5.19	9.81	0.48
Nontronite	Precision	**23.98**	34.50	23.57	**43.84**	23.45	35.23	4.02	9.39
	Recall	9.90	0.45	10.06	0.83	10.18	1.18	**51.26**	**76.06**
	F1-score	14.01	0.90	14.10	1.63	**14.20**	2.28	7.46	**16.72**
All	Precision	**64.32**	**53.79**	61.83	50.32	61.81	48.00	40.11	40.49
	Recall	54.56	34.11	**57.63**	**40.81**	57.49	40.07	45.45	33.33
	F1-score	59.04	41.74	**59.66**	**45.07**	59.57	43.68	42.61	36.56

Although the proposed and alternative methods all showed a decrease in accuracy due to misalignment, method A had a minor decrease in accuracy and the highest precision and recall for many minerals, and the proposed method was the most affected. Since the improved HT method was not affected by misalignment, the mineral map and the accuracy were the same as in Figure 3e and Table 7, respectively.

4. Discussion

In comparison to the MS-based method in the non-overlapping region, all region expansion methods that used the HS image showed higher average F1-scores. This indicates that region expansion of mineral maps using HS images is effective. The validation results using AVIRIS and ASTER images showed that the proposed method had the highest precision for almost all minerals, although the performance of the non-overlap region was lower than that of the overlap region. At the same time, recall was generally higher for the two alternative methods. This is likely because the RF multiclass classifiers of the alternative methods optimized the entire image, resulting in higher precision for minerals

such as chlorite and muscovite, which had more pixels, and lower precision for minerals such as buddingtonite, which had fewer pixels. The proposed method does not depend on the number of pixels of each mineral, and the F1-score calculated from the inter-mineral averages of precision and recall was the highest value, although some minerals showed a significantly lower average F1-score in the expanded region. Minerals with low accuracy in all methods may be due to similarities in spectral shape between minerals [11]. For example, it is clear from the resulting images that nontronite was misestimated as chlorite, and kaolinite was misestimated as alunite. In particular, there are several previous studies on kaolinite and alunite, as both are useful iron-bearing minerals. Pour et al. reported that data from ASTER, Advanced Land Imager (ALI), and Hyperion sensors were used for lithological mapping and ore mineral exploration, but they could not distinguish kaolinite and alunite from other minerals [53]. As for the improved HT method, it had lower accuracy for some minerals, but it would have yielded more accurate results if the number of minerals to be identified had been smaller.

A comparison of the AVIRIS-based mineral map in Figure 3a and the HISUI-based mineral map in Figure 4a shows a significant difference in the distribution of nontronite and generally similar trends for the other minerals. The likely reason for the significant difference in the distribution of nontronite is that the noise in the HISUI image is more significant than that in the AVIRIS image, and the MNF transform suppressed the data around 2.05 μm, where nontronite shows absorption features.

An evaluation of the effect of misalignment between AVIRIS and ASTER images showed that the proposed and alternative methods all decreased in accuracy. Therefore, it is essential to perform the misalignment correction in Step 3. In particular, buddingtonite, which has few pixels, and nontronite and kaolinite, which have many but scattered pixels, are susceptible to misalignment, and the accuracy for these is significantly degraded. On the other hand, the alternative methods work and carry out overall optimization by multiclass classification and have the slightest loss of accuracy due to misalignment and the highest precision and recall for many minerals. If there is a misalignment in HS–MS images, the proposed method is likely to identify first the minerals that are widely distributed and continuous. The reason for this is that the identification error due to misalignment is greater for minerals with small distribution amounts or minerals with scattered distribution. On the other hand, the improved HT method did not show any decrease in accuracy due to misalignment because of its ability to suppress the effect of misalignment. This is due to the ability to search for the best performance of the endmember pixels from the surrounding pixels of the HS endmember [24].

From the above information, we can conclude the following: the proposed method provides more accurate results even for minerals with small distributions because it maps minerals with high confidence. Additionally, because of the high precision, the minerals shown in the obtained maps are expected to be minerals with a high probability. However, since misalignment between HS–MS images causes a decrease in precision, precise alignment is necessary, and depending on the image used, the position correction in Step 3 may be significant. The two alternative methods optimize the overall accuracy of the mineral map by multiclass classification, and thus, the overall accuracy of the mineral map is relatively high. However, the accuracy for minerals present in small amounts tends to deteriorate. The improved HT method is robust against misalignment. However, when the number of minerals to be identified is significant, as in this study case, it becomes difficult to set the threshold of the SAM method automatically, and fine-tuning the threshold for each mineral is necessary to improve accuracy.

The improved forecasting accuracy of the proposed method can be attributed to its hierarchical or cascading approach, in which the classifier is trained sequentially on subsets of classes. The output of each stage is fed into the next, potentially improving the F1-score compared to that from a typical random forest classification. The approach has two main advantages. First, it can reduce class imbalance by training a separate classifier for each target mineral, improving precision values for each stage. Second, it takes

advantage of contextual information by using the previous stages' outputs to guide the next stage's classification. This iterative refinement of classification can potentially reduce misclassifications compared to a single random forest classifier. The hierarchical approach benefits multiclass problems with imbalanced or overlapping classes and can improve the F1-score.

In the proposed method, various mineral indices proposed for the targeted MS sensor are used as RF input candidates, and then unnecessary indices are removed from them based on the RF results. Here, since the candidate mineral indices to be prepared depend on the wavelength and spectral resolution of the MS sensor, it is necessary to consider the candidate mineral indices to be prepared according to the MS sensor to be used. However, since the ASTER used in this study is a typical MS sensor used in geological mapping and has covered most of the Earth's land surface after more than 20 years of observation [54], and since the temporal changes in rocks and minerals are very gradual, adopting the ASTER used in this study as the MS sensor is efficient, and, in this case, the ASTER mineral indices evaluated in this study can be used as candidates.

5. Conclusions

In this study, we proposed a new method to extend the mineral map of HS images by using MS images. The method iteratively performs two-class classification by RF to determine the minerals in order of their consistency within the HS image. The validation results show that the inter-mineral averages of the F1-scores for the overlap and non-overlap regions were 85.98% and 46.46% for the AVIRIS–ASTER image pair and were 82.78% and 42.60% for the HISUI–ASTER image pair, respectively. Although the performance in the non-overlap region was lower than that in the overlap region, the method showed high precision for almost all minerals and high accuracy even for minerals with a few pixels. The comparison between mineral maps generated through multispectral imaging and those based on hyperspectral data showed that using hyperspectral mineral maps as a learning source led to multispectral mineral maps that more closely resembled hyperspectral maps. While existing mineral indices for MS sensors, such as those used in this study, can be calculated by simple arithmetic and applied to various areas, the approach in this study is innovative in that it enables mineral identification that best fits the HS mineral map by integrating these various mineral indices specifically for the area of interest and applying a random forest iteratively while switching minerals. Misalignment between HS–MS images is a factor that degrades accuracy and requires precise alignment. However, the effect of misalignment can be suppressed by the misalignment correction included in the proposed method. Validation studies using different regions and different sensors will be carried out in future works.

Author Contributions: Conceptualization, H.T. (Hideyuki Tonooka); methodology, H.T. (Hideki Tsubomatsu) and H.T. (Hideyuki Tonooka); software, H.T. (Hideki Tsubomatsu); validation, H.T. (Hideki Tsubomatsu); formal analysis, H.T. (Hideki Tsubomatsu); investigation, H.T. (Hideki Tsubomatsu); resources, H.T. (Hideki Tsubomatsu) and H.T. (Hideyuki Tonooka); data curation, H.T. (Hideki Tsubomatsu); writing—original draft preparation, H.T. (Hideki Tsubomatsu); writing—review and editing, H.T. (Hideyuki Tonooka); visualization, H.T. (Hideki Tsubomatsu); supervision, H.T. (Hideyuki Tonooka); project administration, H.T. (Hideyuki Tonooka); funding acquisition, H.T. (Hideyuki Tonooka). All authors have read and agreed to the published version of the manuscript.

Funding: This research received no external funding.

Data Availability Statement: Not applicable.

Acknowledgments: We would like to thank the Geological Survey and Resource Strategy Division, Department of Mines, Industry Regulation and Safety, for their kind assistance in the preparation of Table 5.

Conflicts of Interest: The authors declare no conflict of interest.

References

1. Cudahy, T. Mineral Mapping for Exploration: An Australian Journey of Evolving Spectral Sensing Technologies and Industry Collaboration. *Geosciences* **2016**, *6*, 52. [CrossRef]
2. Sabins, F.F. *Remote Sensing for Mineral Exploration*; Elsevier: Amsterdam, The Netherlands, 1999; Volume 14.
3. Chander, G.; Markham, B.L.; Helder, D.L. Summary of Current Radiometric Calibration Coefficients for Landsat MSS, TM, ETM+, and EO-1 ALI Sensors. *Remote Sens. Environ.* **2009**, *113*, 893–903. [CrossRef]
4. Li, P.; Jiang, L.; Feng, Z. Cross-Comparison of Vegetation Indices Derived from Landsat-7 Enhanced Thematic Mapper plus (ETM+) and Landsat-8 Operational Land Imager (OLI) Sensors. *Remote Sens.* **2013**, *6*, 310–329. [CrossRef]
5. Abrams, M.; Hook, S.J. Simulated ASTER Data for Geologic Studies. *IEEE Trans. Geosci. Remote Sens.* **1995**, *33*, 692–699. [CrossRef]
6. Rowan, L.C.; Mars, J.C. Lithologic Mapping in the Mountain Pass, California Area Using Advanced Spaceborne Thermal Emission and Reflection Radiometer (ASTER) data. *Remote Sens. Environ.* **2003**, *84*, 350–366. [CrossRef]
7. Vural, A.; Akpinar, İ.; Sipahi, F. Mineralogical and Chemical Characteristics of Clay Areas, Gümüşhane Region (NE Turkey), and Their Detection Using the Crósta Technique with Landsat 7 and 8 Images. *Nat. Resour. Res.* **2021**, *30*, 3955–3985. [CrossRef]
8. Koike, K.; Kouda, R. Recent Trends of Remote Sensing Technologies Applied to Metallic Mineral and Geothermal Resources Exploration. *J. MMIJ* **2016**, *132*, 96–113. [CrossRef]
9. Jingu, H.; Kudou, N.; Kashimura, O.; Kato, M.; Abrams, M. Mineral Identification and Quantification for the Practical Use of Satelliteborne Hyperspectral Sensor. *J. Remote Sens. Soc. Jpn.* **2012**, *32*, 300–312.
10. Onuma, T.; Tsukada, M. Geological Interpretation Using Landsat TM Imagery in the Kalpin Uplift, NW Tarim Basin, China. *J. Remote Sens. Soc. Jpn.* **1999**, *19*, 13–28.
11. Mars, J.C.; Rowan, L.C. Spectral Assessment of New ASTER SWIR Surface Reflectance Data Products for Spectroscopic Mapping of Rocks and Minerals. *Remote Sens. Environ.* **2010**, *114*, 2011–2025. [CrossRef]
12. Green, R.O.; Eastwood, M.L.; Sarture, C.M.; Chrien, T.G.; Aronsson, M.; Chippendale, B.J.; Faust, J.A.; Pavri, B.E.; Chovit, C.J.; Solis, M.; et al. Imaging Spectroscopy and the Airborne Visible/Infrared Imaging Spectrometer (AVIRIS). *Remote Sens. Environ.* **1998**, *65*, 227–248. [CrossRef]
13. Guanter, L.; Kaufmann, H.; Segl, K.; Foerster, S.; Rogass, C.; Chabrillat, S.; Kuester, T.; Hollstein, A.; Rossner, G.; Chlebek, C.; et al. The EnMAP Spaceborne Imaging Spectroscopy Mission for Earth Observation. *Remote Sens.* **2015**, *7*, 8830–8857. [CrossRef]
14. Stefano, P.; Angelo, P.; Simone, P.; Filomena, R.; Federico, S.; Tiziana, S.; Umberto, A.; Vincenzo, C.; Acito, N.; Marco, D.; et al. The PRISMA Hyperspectral Mission: Science Activities and Opportunities for Agriculture and Land Monitoring. In Proceedings of the 2013 IEEE International Geoscience and Remote Sensing Symposium-IGARSS, Melbourne, VIC, Australia, 21–26 July 2013; pp. 4558–4561. [CrossRef]
15. Tachikawa, T.; Kashimura, O.; Tanii, J.; Iwasaki, A.; Matsunaga, T.; Tsuchida, S.; Yamamoto, H. Outline and Prospect of Hyperspectral Imager Suite (HISUI). *J. Remote Sens. Soc. Jpn.* **2012**, *32*, 280–286.
16. Cawse-Nicholson, K.; Townsend, P.A.; Schimel, D.; Assiri, A.M.; Blake, P.L.; Buongiorno, M.F.; Campbell, P.; Carmon, N.; Casey, K.A.; Correa-Pabón, R.E.; et al. NASA's Surface Biology and Geology Designated Observable: A Perspective on Surface Imaging Algorithms. *Remote Sens. Environ.* **2021**, *257*, 112349. [CrossRef]
17. Rast, M.; Nieke, J.; Adams, J.; Isola, C.; Gascon, F. COPERNICUS HYPERSPECTRAL IMAGING MISSION FOR THE ENVIRONMENT (CHIME). In Proceedings of the 2021 IEEE International Geoscience and Remote Sensing Symposium IGARSS, Brussels, Belgium, 11–16 July 2021; pp. 108–111. [CrossRef]
18. Kruse, F.A.; Perry, S.L. Regional Mineral Mapping by Extending Hyperspectral Signatures Using Multispectral Data. In Proceedings of the 2007 IEEE Aerospace Conference, Big Sky, MT, USA, 3–10 March 2007; pp. 1–14. [CrossRef]
19. Green, A.A.; Berman, M.; Switzer, P.; Craig, M.D. A Transformation for Ordering Multispectral Data in Terms of Image Quality with Implications for Noise Removal. *IEEE Trans. Geosci. Remote Sens.* **1988**, *26*, 65–74. [CrossRef]
20. Boardman, J.W.; Kruse, F.A.; Green, R.O. Mapping Target Signatures Via Partial Unmixing of AVIRIS Data. In Proceedings of the Summaries of the Fifth Annual JPL Airborne Earth Science Workshop, Pasadena, CA, USA, 23–26 January 1995; Volume 1, pp. 1–95.
21. Yuhas, R.H.; Goetz, A.F.H.; Boardman, J.W. Discrimination among semi-arid landscape endmembers using the spectral angle mapper (SAM) algorithm. In Proceedings of the Summaries of the Third Annual JPL Airborne Geoscience Workshop, Pasadena, CA, USA, 1–5 June 1992; Volume 1.
22. Hirai, A.; Tonooka, H. Mineral Discrimination by Combination of Multispectral Image and Surrounding Hyperspectral Image. *J. Appl. Remote Sens.* **2019**, *13*, 024517. [CrossRef]
23. Hirai, A.; Tonooka, H.; Li, Y. Effectiveness of WorldView-3/SWIR in Mineral Discrimination Using Multispectral Image and Surrounding Hyperspectral Image. *J. Remote Sens. Soc. Jpn.* **2019**, *39*, 307–314.
24. Nakayama, K.; Tonooka, H. Improvement of a Mineral Discrimination Method Using Multispectral Image and Surrounding Hyperspectral Image. *J. Appl. Remote Sens.* **2021**, *15*, 040501. [CrossRef]
25. Alshari, E.A.; Gawali, B.W. Analysis of Machine Learning Techniques for Sentinel-2A Satellite Images. *J. Electr. Comput. Eng.* **2022**, *2022*, 9092299. [CrossRef]
26. Kruse, F.A.; Lefkoff, A.B.; Boardman, J.W.; Heidebrecht, K.B.; Shapiro, A.T.; Barloon, P.J.; Goetz, A.F.H. The Spectral Image Processing System (SIPS)-Interactive Visualization and Analysis of Imaging Spectrometer Data. *Remote Sens. Environ.* **1993**, *44*, 145–163. [CrossRef]

27. Wei, Q.; Bioucas-Dias, J.; Dobigeon, N.; Tourneret, J.-Y.; Chen, M.; Godsill, S. Multi-Band Image Fusion Based on Spectral Unmixing. *IEEE Trans. Geosci. Remote Sens.* **2016**, *54*, 7236–7249. [CrossRef]
28. Kruse, F.A.; Kierein-Young, K.S.; Boardman, W. Mineral Mapping at Cuprite, Nevada with a 63-Channel Imaging Spectrometer. *ISPRS J. Photogramm. Remote Sens.* **1990**, *56*, 83–92.
29. Johnson, K.E.; Koperski, K. Vnir-Swir Superspectral Mineral Mapping: An Example from Cuprite, Nevada. *Photogramm. Eng. Remote Sens.* **2020**, *86*, 695–700. [CrossRef]
30. Ge, W.; Cheng, Q.; Jing, L.; Wang, F.; Zhao, M.; Ding, H. Assessment of the Capability of Sentinel-2 Imagery for Iron-Bearing Minerals Mapping: A Case Study in the Cuprite Area, Nevada. *Remote Sens.* **2020**, *12*, 3028. [CrossRef]
31. Carmon, N.; Thompson, D.R.; Bohn, N.; Susiluoto, J.; Turmon, M.; Brodrick, P.G.; Connelly, D.S.; Braverman, A.; Cawse-Nicholson, K.; Green, R.O.; et al. Uncertainty Quantification for a Global Imaging Spectroscopy Surface Composition Investigation. *Remote Sens. Environ.* **2020**, *251*, 112038. [CrossRef]
32. NASA Jet Propulsion Laboratory. AVIRIS—Airborne Visible Infrared Imaging. Available online: https://aviris.jpl.nasa.gov/ (accessed on 24 April 2023).
33. NASA. AVIRIS Data Portal. Available online: https://aviris.jpl.nasa.gov/dataportal/ (accessed on 24 April 2023).
34. Japan Space Systems. HISUI Hyper-Spectral Imager Suite. Available online: https://www.jspacesystems.or.jp/en/project/observation/hisui/ (accessed on 24 April 2023).
35. AST_07XT v003 ASTER L2 Surface Reflectance VNIR and Crosstalk Corrected SWIR. Available online: https://lpdaac.usgs.gov/products/ast_07xtv003/ (accessed on 24 April 2023).
36. Iwasaki, A.; Tonooka, H. Validation of a Crosstalk Correction Algorithm for ASTER/SWIR. *IEEE Trans. Geosci. Remote Sens.* **2005**, *43*, 2747–2751. [CrossRef]
37. Tonooka, H.; Sakuma, F.; Tachikawa, T.; Kikuchi, M. Radiometric Calibration Status and Recalibration of Aster Thermal Infrared Images. In Proceedings of the IGARSS 2019—2019 IEEE International Geoscience and Remote Sensing Symposium, Yokohama, Japan, 28 July–2 August 2019; pp. 8530–8533. [CrossRef]
38. Tonooka, H. Accurate atmospheric correction of ASTER thermal infrared imagery using the WVS method. *IEEE Trans. Geosci. Remote Sens.* **2005**, *43*, 2778–2792. [CrossRef]
39. Gillespie, A.; Rokugawa, S.; Matsunaga, T.; Cothern, J.S.; Hook, S.; Kahle, A.B. A temperature and emissivity separation algorithm for Advanced Spaceborne Thermal Emission and Reflection Radiometer (ASTER) images. *IEEE Trans. Geosci. Remote Sens.* **1998**, *36*, 1113–1126. [CrossRef]
40. Fujisada, H. Design and performance of ASTER instrument. In Proceedings of the Proceedings Volume 2583, Advanced and Next-Generation Satellites, Paris, France, 25–28 September 1995; Volume 2583, pp. 16–25. [CrossRef]
41. Matthew, M.W.; Adler-Golden, S.M.; Berk, A.; Richtsmeier, S.C.; Levine, R.Y.; Bernstein, L.S.; Acharya, P.K.; Anderson, G.P.; Felde, G.W.; Hoke, M.L.; et al. Status of Atmospheric Correction Using a MODTRAN4-Based Algorithm. In Proceedings of the Proceedings Volume 4049, Algorithms for Multispectral, Hyperspectral, and Ultraspectral Imagery VI, Orlando, FL, USA, 24–28 April 2000; Volume 4049, pp. 199–207.
42. Adler-Golden, S.M.; Matthew, M.W.; Bernstein, L.S.; Levine, R.Y.; Berk, A.; Richtsmeier, S.C.; Acharya, P.K.; Anderson, G.P.; Felde, G.; Gardner, J.; et al. Atmospheric Correction for Short-Wave Spectral Imagery Based on MODTRAN4. In Proceedings of the Proceedings Volume 3753, Imaging Spectrometry V, Denver, CO, USA, 18–23 July 1999; Volume 3753, pp. 61–69. [CrossRef]
43. Bierwirth, P.N. Evaluation of ASTER satellite data for geological applications. Consultancy Report to Geoscience Australia. 2002; 50 p, unpublished.
44. Rowan, L.C.; Hook, S.J.; Abrams, M.J.; Mars, J.C. Mapping Hydrothermally Altered Rocks at Cuprite, Nevada, Using the Advanced Spaceborne Thermal Emission and Reflection Radiometer (ASTER), A New Satellite-Imaging System. *Econ. Geol.* **2003**, *98*, 1019–1027. [CrossRef]
45. Gozzard, J.R. *Image Processing of ASTER Multispectral Data*; Geological Survey of WA: East Perth, WA, Australia, 2006.
46. Rajendran, S.; Nasir, S. ASTER Capability in Mapping of Mineral Resources of Arid Region: A Review on Mapping of Mineral Resources of the Sultanate of Oman. *Ore Geol. Rev.* **2019**, *108*, 33–53. [CrossRef]
47. Volesky, J.C.; Stern, R.J.; Johnson, P.R. Geological Control of Massive Sulfide Mineralization in the Neoproterozoic Wadi Bidah Shear Zone, Southwestern Saudi Arabia, Inferences from Orbital Remote Sensing and Field Studies. *Precambrian Res.* **2003**, *123*, 235–247. [CrossRef]
48. Hewson, R.D.; Cudahy, T.J.; Huntington, J.F. Geologic and Alteration Mapping at Mt Fitton, South Australia, Using ASTER Satellite-Borne Data. Scanning the Present and Resolving the Future. In Proceedings of the IEEE 2001 International Geoscience and Remote Sensing Symposium, Sydney, NSW, Australia, 9–13 July 2001; Volume 2, pp. 724–726.
49. Ninomiya, Y. Mapping Quartz, Carbonate Minerals, and Mafic-Ultramafic Rocks Using Remotely Sensed Multispectral Thermal Infrared ASTER Data. In Proceedings of the Thermosense XXIV, Orlando, FL, USA, 1–5 April 2002; Volume 4710, pp. 191–202.
50. Sengar, V.K.; Venkatesh, A.S.; Champati ray, P.K.; Sahoo, P.R.; Khan, I.; Chattoraj, S.L. Spaceborne Mapping of Hydrothermal Alteration Zones Associated with the Mundiyawas-Khera Copper Deposit, Rajasthan, India, Using SWIR Bands of ASTER: Implications for Exploration Targeting. *Ore Geol. Rev.* **2020**, *118*, 103327. [CrossRef]
51. Gabr, S.; Ghulam, A.; Kusky, T. Detecting Areas of High-Potential Gold Mineralization Using ASTER Data. *Ore Geol. Rev.* **2010**, *38*, 59–69. [CrossRef]

52. Pour, A.B.; Hashim, M.; Hong, J.K.; Park, Y. Lithological and Alteration Mineral Mapping in Poorly Exposed Lithologies Using Landsat-8 and ASTER Satellite Data: North-Eastern Graham Land, Antarctic Peninsula. *Ore Geol. Rev.* **2019**, *108*, 112–133. [CrossRef]
53. Pour, A.B.; Hashim, M. ASTER, ALI and Hyperion Sensors Data for Lithological Mapping and Ore Minerals Exploration. *Springerplus* **2014**, *3*, 130.
54. Abrams, M.; Yamaguchi, Y. Twenty Years of ASTER Contributions to Lithologic Mapping and Mineral Exploration. *Remote Sens* **2019**, *11*, 1394. [CrossRef]

Disclaimer/Publisher's Note: The statements, opinions and data contained in all publications are solely those of the individual author(s) and contributor(s) and not of MDPI and/or the editor(s). MDPI and/or the editor(s) disclaim responsibility for any injury to people or property resulting from any ideas, methods, instructions or products referred to in the content.